

Transparent and Flexible Self-Charging Power Film and Its Application in a Sliding Unlock System in Touchpad Technology

Jianjun Luo,^{†,‡} Wei Tang,^{†,‡} Feng Ru Fan,[†] Chaofeng Liu,[†] Yaokun Pang,[†] Guozhong Cao,^{†,‡} and Zhong Lin Wang^{*,†,§}

[†]Beijing Institute of Nanoenergy and Nanosystems, Chinese Academy of Sciences, National Center for Nanoscience and Technology (NCNST), Beijing 100083, China

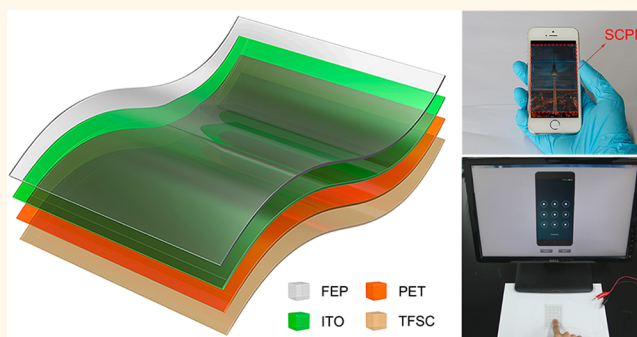
[‡]Department of Materials Science and Engineering, University of Washington, Seattle, Washington 98195, United States

[§]School of Materials Science and Engineering, Georgia Institute of Technology, Atlanta, Georgia 30332, United States

Supporting Information

ABSTRACT: Portable and wearable personal electronics and smart security systems are accelerating the development of transparent, flexible, and thin-film electronic devices. Here, we report a transparent and flexible self-charging power film (SCPF) that functions either as a power generator integrated with an energy storage unit or as a self-powered information input matrix. The SCPF possesses the capability of harvesting mechanical energy from finger motions, based on the coupling between the contact electrification and electrostatic induction effects, and meanwhile storing the generated energy. Under the fast finger sliding, the film can be charged from 0 to 2.5 V within 2094 s and discharge at 1 μ A for approximately 1630 s. Furthermore, the film is able to identify personal characteristics during a sliding motion by recording the electric signals related to the person's individual bioelectricity, applied pressing force, sliding speed, and so on, which shows its potential applications in security systems in touchpad technology.

KEYWORDS: transparent and flexible, self-charging, energy storage, energy harvesting, biometrics



Transparent, flexible, and thin-film electronics are a recent focus of scientific research for their applications in personal devices (such as mobile phones, wearable electronics), smart windows, security systems, optical coatings, and so on.^{1–5} Definitely, they all need an external power source to operate. Rapid advancement in the development of the triboelectric nanogenerator (TENG),^{6–8} which includes theoretical modeling,^{9,10} experimental demonstrations,^{11–13} and material optimization,^{14–16} has generated a concept of self-powering/charging technology.^{17–20} It enables mechanical energy harvesting based on a transparent and flexible configuration.^{21–24} However, to be applied in our daily electronics, the device requires a high degree of integration and 3D motion energy scavenging ability; moreover, the as-generated scattered energy also needs to be stored properly.

In this work, a transparent and flexible self-charging power film (SCPF) is presented. By embedding a grid-like indium tin oxide (ITO) electrode below a fluorinated ethylene propylene (FEP) film, both contacting and sliding mechanical energy can be harvested based on the coupling between the contact

electrification and electrostatic induction effects.^{25,26} To store the scattered energy, all-solid-state transparent and flexible supercapacitors (TFSCs) based on interdigital electrodes of 3D Au@MnO₂ nanocomposites are fabricated and connected to form an array on the backside of the nanogenerator. By simply applying finger motions on the surface, an open-circuit voltage of 31.5 V, and a short-circuit current of 224 nA are achieved by the TENG, and an areal capacitance of 1.30 mF/cm² is obtained by the supercapacitor at a current density of 2 μ A/cm². After mechanical energy harvesting and storing, the SCPF can successfully drive a calculator. In addition, the film is utilized as an intelligent sliding unlock system, where it is able to identify personal characteristics during sliding by recording the electric signals related to the person's individual bioelectricity, applied pressing force, sliding speed, and so on.

Received: June 24, 2016

Accepted: August 8, 2016

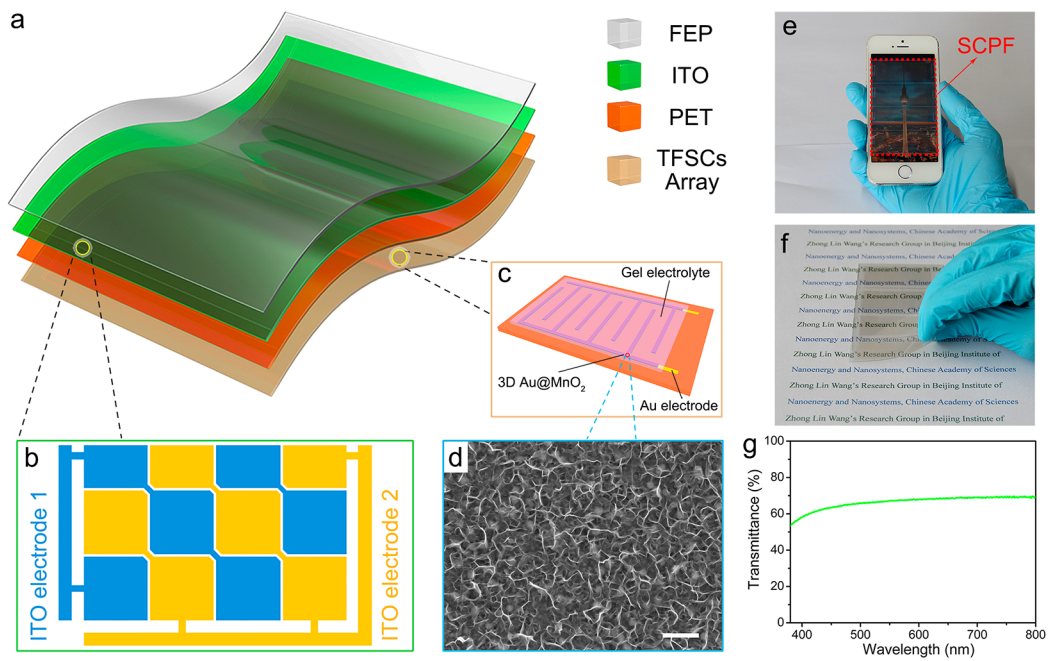


Figure 1. Structural design of the transparent and flexible SCPF. (a) Schematic illustration of the transparent and flexible SCPF. (b) Enlarged schematic of the TENG's electrode layer. (c) Schematic diagram of a single TFSC device architecture. (d) SEM image of the 3D Au@MnO₂ nanocomposites. Scale bar, 500 nm. (e, f) Photographs of a SCPF demonstrate its transparency and flexibility. (g) Transmittance spectra of the SCPF.

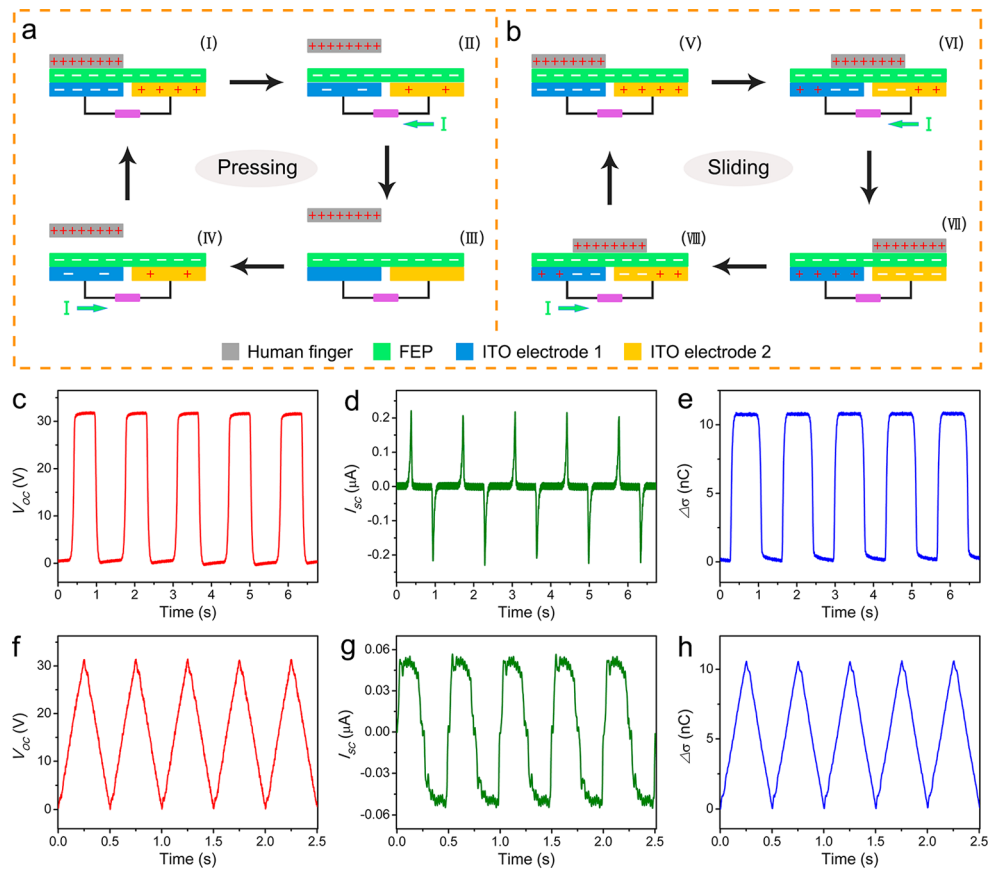


Figure 2. Working mechanisms and output performance of the transparent and flexible TENG in different modes. (a) Working mechanism of TF-TENG in contact-separation mode. (b) Working mechanism of TF-TENG in sliding mode. (c–e) Open-circuit voltage (V_{OC}), short-circuit current (I_{SC}), and transferred charge ($\Delta\sigma$) of the TF-TENG in contact-separation mode, measured by using a linear motor for triggering the device. (f–h) V_{OC} , I_{SC} , and $\Delta\sigma$ of the TF-TENG in sliding mode at a sliding velocity of 0.04 m/s.

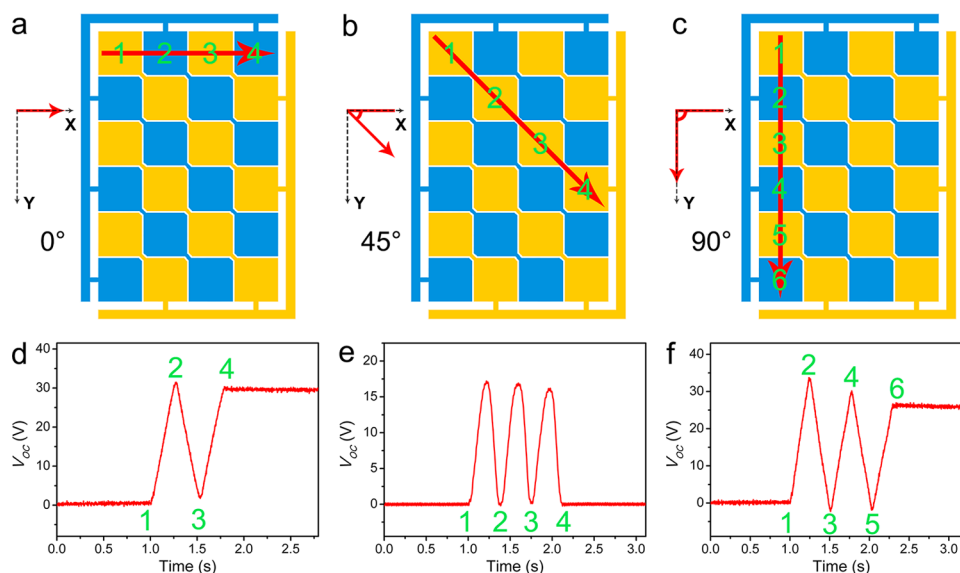


Figure 3. Output performance of the transparent and flexible TENG along different sliding directions. Schematic illustrations of the typical sliding paths when the sliding angle is (a) 0° , (b) 45° , and (c) 90° . Output voltage of the TF-TENG in typical sliding paths when the sliding angle is (d) 0° , (e) 45° , and (f) 90° .

Therefore, we believe that our demonstration of the transparent and flexible self-charging power film will have a wide variety of applications for portable, wearable, and smart electronics in the future.

RESULTS AND DISCUSSION

Device Configuration. The SCPF is composed of several vertically stacked transparent thin films. As depicted in Figure 1a, a layer of ITO was patterned as grids (Figure 1b) and attached on the polyethylene terephthalate (PET). The process for fabricating the patterned ITO is illustrated in the Methods section and Supporting Information Figure S1. Then, a layer of FEP was covered on the ITO electrodes, serving as an electrification layer that generates triboelectric charges upon contact with human fingers. Thus, a transparent and flexible triboelectric nanogenerator (TF-TENG) is formed. Below it, an all-solid-state TFSC array based on interdigital electrodes of 3D Au@MnO₂ nanocomposites was fabricated as the energy storage component to gather the TENG's output energy. An enlarged structure of a single TFSC is shown in Figure 1c, and the detailed fabrication process is illustrated in the Methods section and Figure S2. A scanning electron microscopy (SEM) image of the 3D Au@MnO₂ is displayed in Figure 1d, suggesting the conformal coating of 3D Au nanostructures with hierarchical MnO₂ nanosheets. Photographs of the SCPF are shown in Figure 1e,f, plainly demonstrating its transparency, flexibility, and integral one-piece structure. The high transmittance of the SCPF is evident in Figure 1g, which shows an optical transmittance of 67.1% at a wavelength of 550 nm.

Electricity Generation. Two parts of mechanical energy are provided by finger movements. One is pressing, and the other is sliding. In order to harvest both of them, our TF-TENG is designed to work in contact-separation mode and sliding mode simultaneously. The working mechanism for the pressing is illustrated in Figure 2a. As a human finger makes contact with the FEP film, due to their different abilities in attracting electrons, there will be positive triboelectric charges on the human skin and negative ones on the FEP. Therefore, when the positive charged human finger approaches the ITO

electrode 1, the ITO electrode 1 possesses a higher electrical potential than the ITO electrode 2, leading to an instantaneous electron flow from the ITO electrode 2 to ITO electrode 1 (II), finally reaching equilibrium until the finger and the FEP film are contacted (III). Once the finger separates, electrons flow backward from the ITO electrode 1 to ITO electrode 2 (IV), until achieving another equilibrium (I).

For the sliding mode, the mechanism is illustrated in Figure 2b. When the positive charged human finger starts to slide toward the right-hand side, the induced positive charges on the ITO electrode 2 are expelled, resulting in a flow of electrons from the ITO electrode 1 to ITO electrode 2 (VI), finally reaching equilibrium when the finger continuously moves forward and stops on the right side of the FEP (VII). Once the finger moves back from the right side to the left side, the electrons flow back from ITO electrode 2 to ITO electrode 1 (VIII), until achieving another equilibrium (V).

Subsequently, the output performance of the TF-TENG in two working modes was evaluated. For the contact-separation mode, the open-circuit voltage (V_{OC}), short-circuit current (I_{SC}), and transferred charge ($\Delta\sigma$) of the TF-TENG are shown in Figure 2c–e, with peak values of around 31.5 V, 224 nA, and 10.8 nC, respectively. Meanwhile, the output performance of the TF-TENG in sliding mode was characterized at a sliding velocity of 0.04 m/s. As exhibited in Figure 2f–h, the peak values of V_{OC} and $\Delta\sigma$ are very similar to those in the contact-separation mode. However, the I_{SC} is much smaller than that in the contact-separation mode, with a peak value of 55.1 nA, which can be attributed to the different movement speeds in two modes.²⁷ As a supplement, we investigated the output current of the TF-TENG in different sliding velocity, which is shown in Figure S3. Furthermore, the TF-TENG shows a high optical transmittance of 82.2% at a wavelength of 550 nm (Figure S4).

Moreover, our TF-TENG can harvest the sliding energy from all directions with a grid-like ITO electrode structure design. In the consideration of the symmetric and periodic arrangement of the electrodes, we investigated the output performance of the TF-TENG in three typical sliding angles (0,

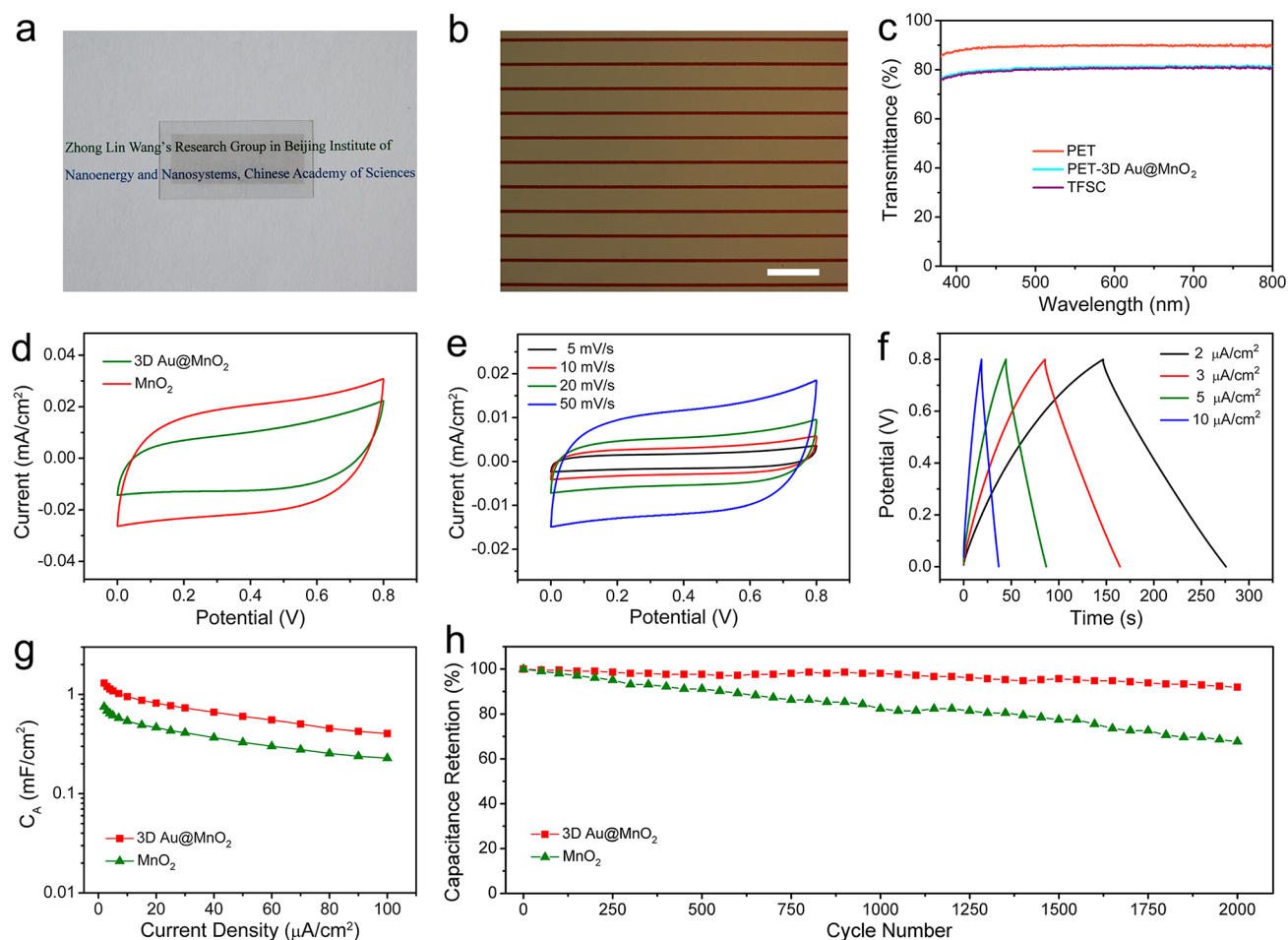


Figure 4. Electrochemical performance of a single all-solid-state TFSC. (a) Photograph of the TFSC on a piece of paper printed with the BINN logo (used with permission). (b) Optical microscope image of the TFSC shows interdigital electrodes. Scale bar, 200 μm . (c) Transmittance spectra of pure PET, PET-3D Au@MnO₂ and an assembled TFSC. (d) Cyclic voltammetry (CV) curves of the TFSCs based on 3D Au@MnO₂ and pristine MnO₂ at a scan rate of 100 mV/s. (e) CV curves of TFSCs at scan rates of 5, 10, 20, and 50 mV/s. (f) Galvanostatic charge–discharge (CC) curves of TFSCs at current densities of 2, 3, 5, and 10 $\mu\text{A}/\text{cm}^2$. (g) Specific areal capacitances (C_A) of TFSCs based on 3D Au@MnO₂ and pristine MnO₂ calculated from CC curves as a function of the current density. (h) Cycling stability of TFSCs based on 3D Au@MnO₂ and pristine MnO₂ at the current density of 30 $\mu\text{A}/\text{cm}^2$.

45, and 90°), under the sliding velocity of 0.04 m/s. The sliding paths are illustrated in Figure 3a–c. Related voltage outputs are in Figure 3d–f (the number corresponds to the position in the sliding paths). When the finger slides along the *X* axis (Figure 3a), the induction electrode varied three times, and thus the voltage shifted between 0 and the top value in the same manner (Figure 3d). It can also be seen in the movement along the *Y* axis (Figure 3c,f). For the movement in the 45° angle, the biggest mismatch occurred between two grids, corresponding to the peak of the voltage in Figure 3e. Since the mismatch area is about one-half of a grid area, the peak value is around 15–18 V. In order to visually demonstrate the advantage of our structure design, eight light-emitting diodes could be lighted by all-direction motions including both pressing and sliding (Supporting Information Video S1).

Energy Storage. The energy storage unit is made up of a supercapacitor array. To ensure the transparency of the whole SCPF, a promising approach is using the micropatterned electrode structure for the supercapacitor, covering only a small fraction of the whole device.^{28,29} Herein, we utilized the interdigital electrode structure for the TFSC, with its line width of $\sim 10 \mu\text{m}$ and interspace of $\sim 90 \mu\text{m}$ (Figure 4b). Figure 4a

shows a photograph of one single TFSC on a piece of paper. The distinct BINN logo demonstrated the transparent nature of our TFSC. The transparency of the TFSC was measured and is exhibited in Figure 4c. At a wavelength of 550 nm, the TFSC processed an optical transmittance of approximately 80.4%. The excellent transparency of the TFSC can be attributed to its highly transparent components of PET substrate with a transmittance of 90%, the electrolyte with negligible transmittance reduction, and the in-plane interdigital electrode structure design.

For active materials, MnO₂ is considered to be the most attractive oxide material due to its remarkable theoretical specific capacitance, natural abundance, low cost, and environmental friendliness.^{30–32} However, considering its poor conductivity, which remains a major challenge and limits the rate capabilities for high-power performance,^{33,34} we incorporated the MnO₂ onto the highly conductive Au nanostructures to form a 3D Au@MnO₂ nanostructure composite by using a facile electrochemical deposition process. The surface topography of the 3D Au nanostructures was first optimized by changing the deposition conditions (Figures S5 and S6). To evaluate the electrochemical performance of the 3D Au@

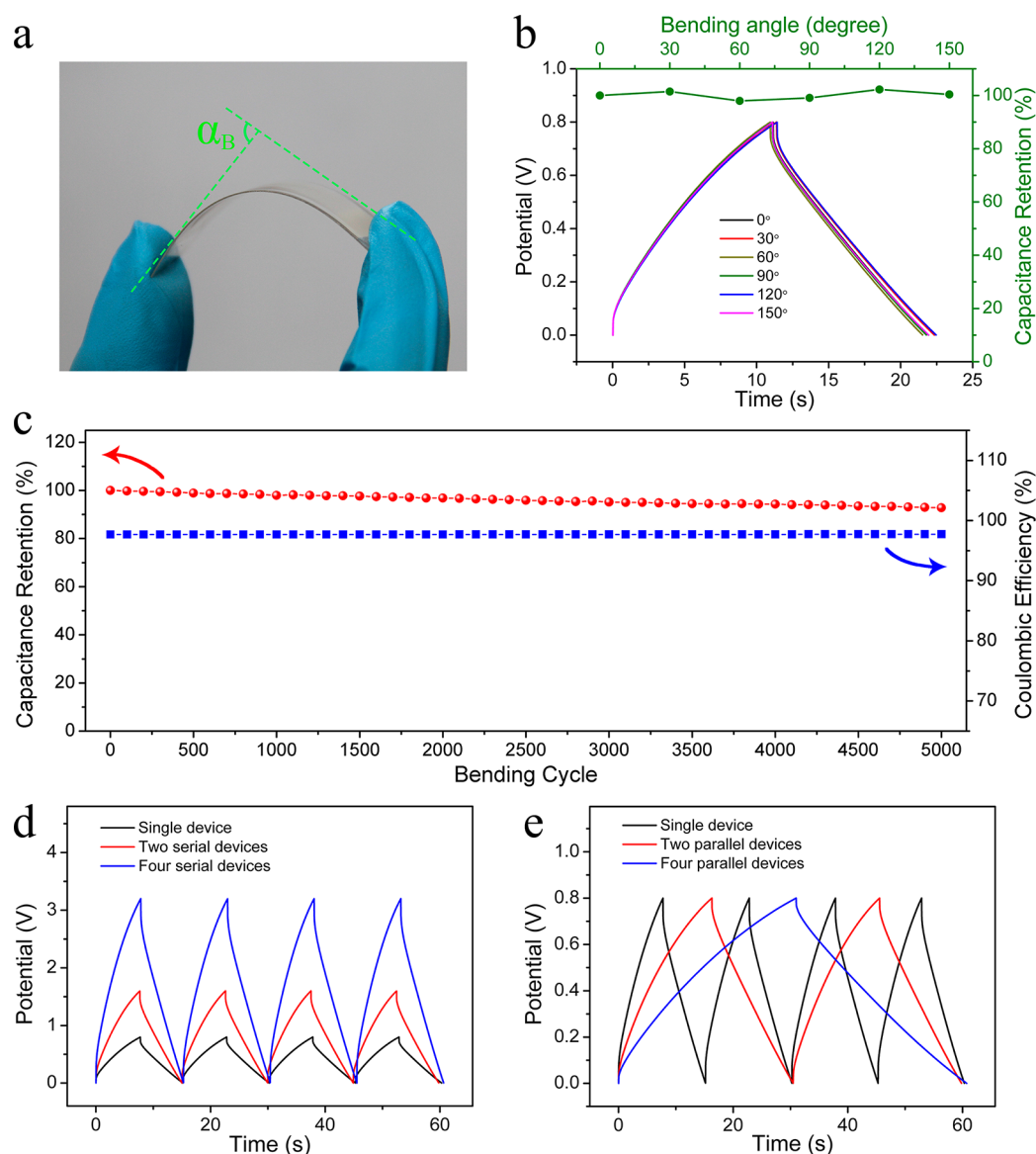


Figure 5. Flexibility testing of the TFSC. (a) Photograph of a device under bending. The angle labeled as α_B in the image is defined as the bending angle. (b) Galvanostatic CC curves and capacitance retention of the TFSC under bending angles of 0, 30, 60, 90, 120, and 150° at the current density of $15 \mu\text{A}/\text{cm}^2$. (c) Capacitance retention of TFSC at different bending cycles with an α_B of $\approx 90^\circ$. Galvanostatic CC curves for two and four TFSCs connected (d) in series and (e) in parallel. A single TFSC is shown for comparison. Both the tandem devices and the single device were operated at the same constant current charge/discharge.

MnO_2 -based TFSC, cyclic voltammetry (CV) and galvanostatic charge–discharge (CC) measurements were performed. Figure 4d shows the CV curves of pristine MnO_2 and 3D $\text{Au}@\text{MnO}_2$ -based TFSCs at a scan rate of 100 mV/s. It is evident that the 3D $\text{Au}@\text{MnO}_2$ -based TFSC reveals much higher capacitive current density, indicating that the electrochemical performance can be improved by introducing 3D Au nanostructures. It is also worth noting that the CV curve of 3D $\text{Au}@\text{MnO}_2$ -based TFSC shows a more quasi-rectangular shape, suggesting its good capacitive behavior and high-rate capability.

In addition, Figure 4e shows the CV curves of 3D $\text{Au}@\text{MnO}_2$ -based TFSCs at varying scan rates from 5 to 50 mV/s. The CV curves maintain their quasi-rectangular shapes, and this is suggestive of good electrochemical double-layer stability. This excellent capacitive behavior is further confirmed by the nearly triangular CC curves at current densities ranging from 2 to $10 \mu\text{A}/\text{cm}^2$ (Figure 4f). Additional CV curves at higher scan

rates and CC curves at higher current densities are plotted in Figure S7 to show that 3D $\text{Au}@\text{MnO}_2$ -based TFSC can be charged and discharged over a wide range of scan rates (5 to 1000 mV/s) and current densities (2 to $50 \mu\text{A}/\text{cm}^2$). The calculated specific areal capacitances (C_A) from the CC curves with its corresponding current densities are shown in Figure 4g, demonstrating that the 3D $\text{Au}@\text{MnO}_2$ -based TFSC exhibited significantly enhanced capacitance performance, with C_A as high as $1.30 \text{ mF}/\text{cm}^2$ achieved at a current density of $2 \mu\text{A}/\text{cm}^2$, $\sim 74\%$ increase compared with the pristine MnO_2 electrode. This value is fairly comparable or superior to previously reported carbon nanotubes^{35,36} or graphene^{37,38}-based TFSCs while keeping a high device transparency.

Good cycling stability is another important characteristic for high-performance supercapacitors. Figure 4h reveals the cycle performance of the TFSCs based on 3D $\text{Au}@\text{MnO}_2$ and pristine MnO_2 measured at $30 \mu\text{A}/\text{cm}^2$ for 2000 cycles. After

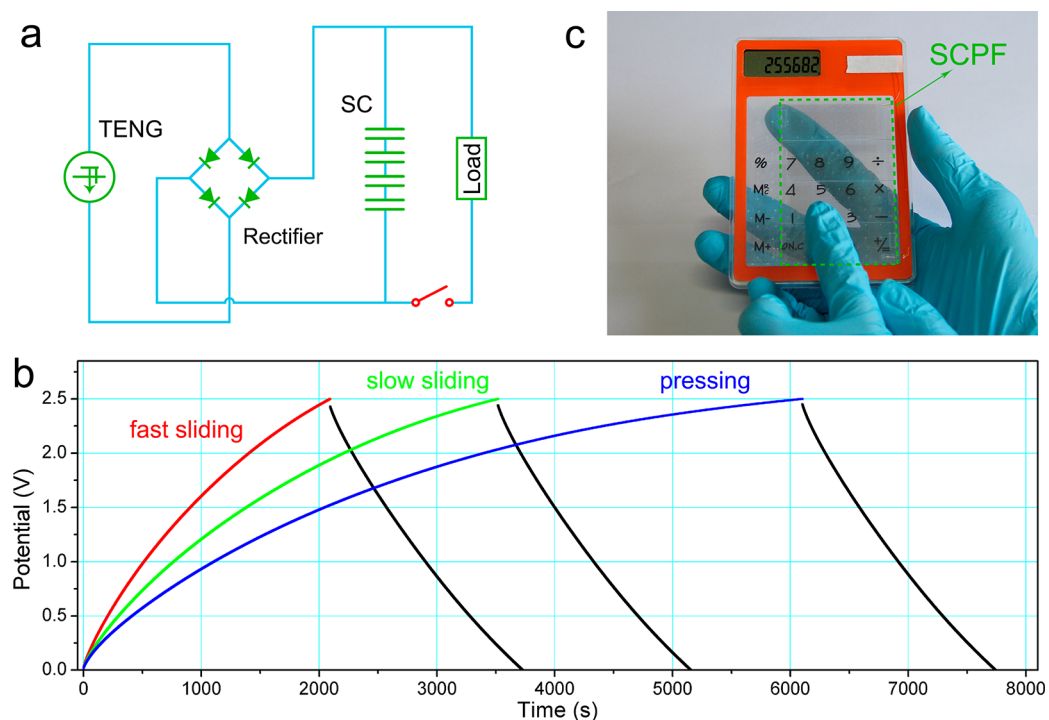


Figure 6. Performance of the transparent and flexible SCPF. (a) Circuit diagram of the transparent and flexible SCPF. (b) Charging curves of four TFSCs in series charged by the TF-TENG at fast sliding (red line), slow sliding (green line), and pressing (blue line) and discharged at $1 \mu\text{A}$ (black line). (c) Photograph of a calculator driven by the SCPF.

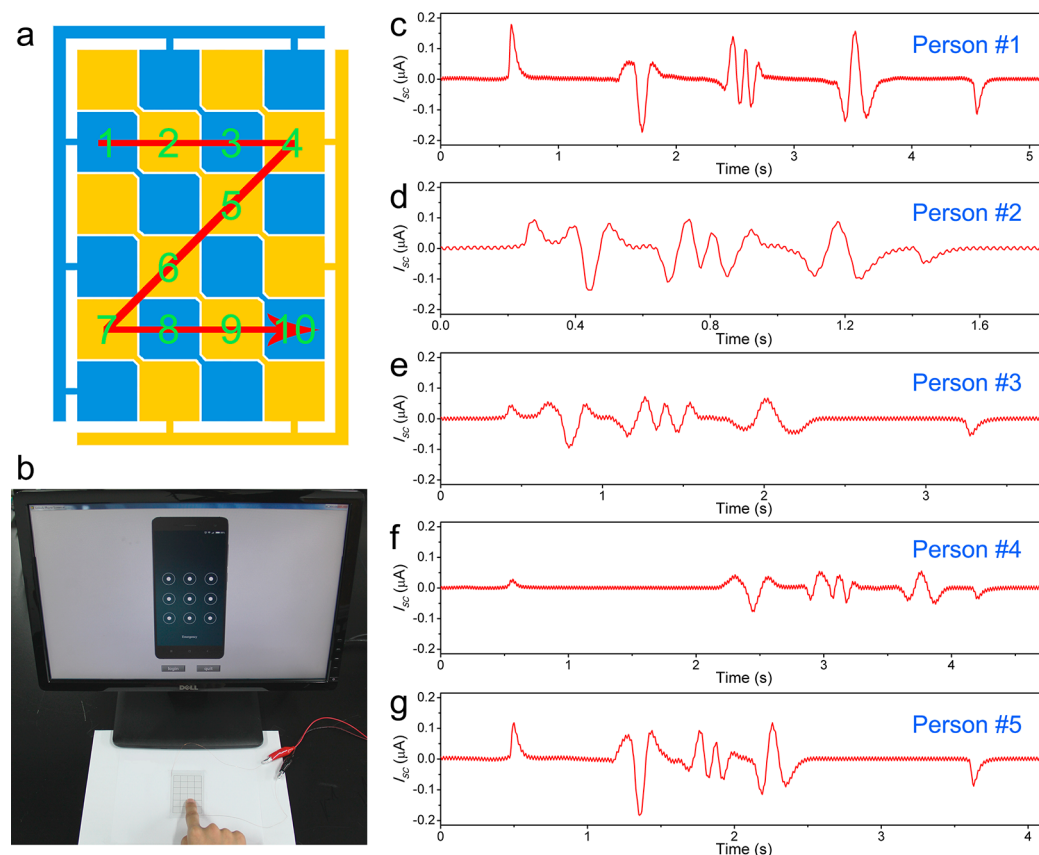


Figure 7. Intelligent sliding unlock system. (a) Schematic illustration of the preset sliding password. (b) Photograph of the intelligent sliding unlock system. (c–g) Output current signals of five different people.

2000 cycles of the charge–discharging test, the capacitance of 3D Au@MnO₂-based TFSC remained ~92%, showing much better cycling performance compared to pristine MnO₂-based TFSC (68% retention after 2000 cycles). These excellent electrochemical properties of the 3D Au@MnO₂-based TFSC might be ascribed to the high electric conductivity of the 3D Au nanostructures, high porosity, and large specific surface area of the 3D Au@MnO₂ nanocomposites, which facilitate electrolyte diffusion, electron transport, and material utilization.³³ A Ragone plot of a single TFSC with areal energy density and power density is also provided in Figure S8 to better evaluate its commercial application potential.

By varying the line width and interspace in the interdigital electrode, we fabricated supercapacitors with lower transparency of 71.5 and 62.6%, as demonstrated in Figure S9, but the corresponding C_A increased to 2.66 and 4.12 mF/cm². Therefore, there could be a trade off in the practical applications. Table S1 compares the capacitance and transmittance of various transparent and flexible supercapacitors.

The flexibility of a supercapacitor based on 3D Au@MnO₂ was also studied (Figure 5). The digital image of a TFSC device that is manually bent with a bending angle (α_B) of $\approx 90^\circ$ is shown in Figure 5a. The CC curves at different α_B are essentially superimposable, and the calculated capacitance remains almost the same, indicating that the device could be bent to a large extent without degrading the performance (Figure 5b). A long-term stability test was carried out by bending the device with an α_B of $\approx 90^\circ$ (Figure 5c). The performance of the TFSC device was confirmed to be very stable (~7% degradation), while maintaining high Coulombic efficiency (~98%) throughout the cycles, implying a good mechanical flexibility of the TFSC system. This superior performance makes the supercapacitor from 3D Au@MnO₂ promising for transparent, flexible, and portable electronics.

In order to meet the specific energy and power needs for practical applications, multiple TFSCs based on 3D Au@MnO₂ can also be connected in either series or parallel configurations (Figure 5d,e). Compared with a single TFSC, the voltage windows of two and four TFSCs connected in series increased by a factor of 2 and 4 with similar charge/discharge time. When two and four TFSCs were connected in parallel, the output currents increased to 2 \times and 4 \times that of a single TFSC, suggesting correspondingly enhanced capacitance. Such controllable operating voltage window and capacity by simple serial and parallel connections could facilitate their practical applications as energy storage devices.

Devices Integration. Simply connecting the TENG with a TFSC array (four supercapacitors connected in series), a whole transparent and flexible self-charging power film was fabricated. The electrical connection of the SCPF is displayed in Figure 6a. The SCPF can convert the mechanical energy of finger motions to electrical energy and stores it in the TFSC array component. As shown in Figure 6b, the SCPF was charged by different kinds of finger motions. For the finger tapping, the SCPF was charged from 0 to 2.5 V within 6102 s (blue line) and galvanostatically discharged at 1 μ A for 1639 s. When the finger motion becomes slow sliding (0.5 m/s) and fast sliding (0.8 m/s), the charging time can be shortened to 3518 s (green line) and 2094 s (red line), and the following discharging at 1 μ A still lasts for approximately 1630 s. As a demonstration, the SCPF was successfully used to drive a scientific calculator sustainably (Figure 6c).

Intelligent Sliding Unlock System. Furthermore, the transparent and flexible SCPF was utilized to investigate a person's sliding characteristics. Five people were invited independently to slide a "Z" on the SCPF (Figure 7a). Figure 7c–g shows the five output current signals obtained by these individuals. It is clear that five signals are distinguished from each other. These signals correlate to a variety of information, including the manner of the sliding, finger size, individual bioelectricity, applied pressing force, and sliding speed. Therefore, each current signal produced in the sliding process by each person has its own unique characteristic, including the number of current peaks, intensity of each peak signal, and the time interval between each two continuous peak signal. After signal processing, features of the above five signals are extracted and provided in Table S2. Knowing that, we employed the SCPF as an additional layer of stronger security to the present sliding authentication system, building up an intelligent sliding unlock system (ISUS) (Figure 7b and Video S2). When three people slid through the ISUS, even the preset sliding password is known, only the genuine owner with matched sliding characteristics can access the system, demonstrating the feasibility of our ISUS.

CONCLUSIONS

In summary, we have presented a transparent and flexible self-charging power film. The film can charge itself from human finger motions, including tapping and sliding from all directions, by the coupling effect of contact electrification and electrostatic induction and storing the as-generated energy in a 3D Au@MnO₂-based supercapacitor array. In addition, it can be used to drive mobile electronics. Given that cell phones, tablets, e-readers, netbooks, and other portable electronic devices have been widely used in daily life, the wasted mechanical energy can be effectively harvested when using them.

Furthermore, an intelligent sliding unlock system was built as a biometric authentication system, due to the fact that the triboelectric signals by the human sliding motions relate to a lot of personalities, including the manner and rhythm of the sliding, finger size, individual bioelectricity, applied pressing force, sliding speed, and so forth. Remarkably, the SCPF demonstrated herein features a variety of advantages such as being chemically and mechanically stable, simple, cost-effective, and lightweight and can be easily implemented as an additional layer on various mobile electronics. This work is a milestone in self-powered systems and security systems and may have significant implications on the future technology.

METHODS

Fabrication of the TF-TENG. A negative photoresist layer was first spin-coated and developed on a transparent PET–ITO substrate (Aldrich) using a photomask (MA-6, Karl-suss). Subsequently, ITO etching was performed using HCl/HNO₃/H₂O = 50:3:50 as etchant. The remaining photoresist was then removed with acetone to generate the desired ITO pattern on the PET. Finally, a layer of FEP film was pasted on the patterned ITO as the electrification layer. It is worth noting that the size of a single grid ITO electrode is 1 \times 1 cm².

Synthesis of 3D Au@MnO₂ Films. First, the PET substrates were ultrasonically cleaned in acetone, ethanol, and deionized (DI) water for 30 min each. Standard photolithography was subsequently conducted to generate the desired pattern on the PET substrates. Next, a current collector consisting of 10 nm Cr and 70 nm Au was sequentially deposited onto the substrates (Denton Sputter). For electrodeposition of 3D Au@MnO₂, the films were first immersed into

the 5 mM HAuCl₄ (Sigma-Aldrich) solutions in different pH values. Their pH values were adjusted to a fixed value with HCl and NaOH solution and were aged for about 12 h. Au nanostructures were electrodeposited at a constant potential of 0.5 V (*vs* Ag/AgCl) at room temperature for 400 s. Thereafter, the films with Au nanostructures were washed with DI water and dried in the air, immersed into the manganese acetate plating solution containing 20 mM Mn(CH₃COO)₂ (Sigma-Aldrich) and 10 mM NH₄(CH₃COO)₂ (Sigma-Aldrich), and subjected to 15 min deposition under constant potential of 0.6 V (*vs* Ag/AgCl). The remaining photoresist was lifted off with acetone followed by an overnight drying at room temperature and pressure. Electrodeposition of 3D Au@MnO₂ was achieved with a three-electrode setup. Besides the working electrode, a Ag/AgCl electrode and a platinum plate served as reference electrode and counter electrode, respectively.

Fabrication of the All-Solid-State TFSCs. The LiCl/PVA polymer gel electrolyte was prepared by stirring 20 mL of DI water, 0.5 g of LiCl (Sigma-Aldrich), and 2.0 g of PVA (*M_w* = 50 000, Aldrich No. 34158-4) at 80 °C for 2 h. Approximately, 0.4 mL of the electrolyte was applied to the active area of the 3D Au@MnO₂ films, followed by placing the devices overnight in a vacuum desiccator for further solidification of the electrolyte.

Characterization and Measurement. SEM images were taken using a Hitachi SU8020 FE-SEM. Optical images were obtained using a Zeiss Axio Imager M2 microscopy. The open-circuit voltage and transferred charge signals of the TENG were measured by a programmable electrometer (Keithley System 6514). The short-circuit current signals of the TENG were determined by a low-noise current preamplifier (Stanford Research SR570). CV and galvanostatic CC measurements were performed using an electrochemical workstation (CHI 660E). The optical transmittances of the TFSCs were measured by a Shimadzu UV-3600 spectrometer equipped with an integrating sphere.

Calculations. All electrochemical performances of the TFSCs were tested in a two-electrode configuration with LiCl/PVA as the solid electrolyte.

The areal specific capacitance of electrode materials was calculated from galvanostatic charge–discharge curves according to eq 1:

$$C_A = 4I / (A_{\text{device}} \times (dV/dt)) \quad (1)$$

where *I* is the discharge current, *A_{device}* is the total area of the device (including the area of microelectrodes and the interspaces between them), and *dV/dt* is the slope of the discharge curve.

The areal capacitance (*C_{device,A}*) of the TFSCs was calculated using eq 2:

$$C_{\text{device,A}} = C_A / 4 \quad (2)$$

The areal energy density (*E_{device,A}*) and power density (*P_{device,A}*) of the TFSCs were calculated using eqs 3 and 4, respectively:

$$E_{\text{device,A}} = C_{\text{device,A}} (\Delta V)^2 / (2 \times 3600) \quad (3)$$

$$P_{\text{device,A}} = E_{\text{device,A}} \times 3600 / \Delta t \quad (4)$$

where ΔV is the discharge potential range after the IR drop and Δt is the discharge time.

ASSOCIATED CONTENT

Supporting Information

The Supporting Information is available free of charge on the ACS Publications website at DOI: 10.1021/acs.nano.6b04201.

Supporting figures and tables (PDF)

Video S1 (AVI)

Video S2 (AVI)

AUTHOR INFORMATION

Corresponding Author

*E-mail: zlwang@gatech.edu.

Author Contributions

[†]J.L. and W.T. contributed equally to this work.

Notes

The authors declare no competing financial interest.

ACKNOWLEDGMENTS

This research was supported by the “thousands talents” program for pioneer researcher and his innovation team, China, National Natural Science Foundation of China (Grant Nos. 51432005, 5151101243, 51561145021, 61504009, and 21403181), and Beijing Natural Science Foundation of China (Grant No. 4141002). Patents have been filed based on the research results presented in this article. The authors thank Fei Xue, Xun Han, Jian Chen, Chao Yuan, and Cunxin Lu for their help in this work.

REFERENCES

- (1) Wang, L.; Yoon, M. H.; Lu, G.; Yang, Y.; Facchetti, A.; Marks, T. J. High-Performance Transparent Inorganic–Organic Hybrid Thin-Film n-Type Transistors. *Nat. Mater.* **2006**, *5*, 893–900.
- (2) Kim, K. S.; Zhao, Y.; Jang, H.; Lee, S. Y.; Kim, J. M.; Kim, K. S.; Ahn, J.-H.; Kim, P.; Choi, J. Y.; Hong, B. H. Large-Scale Pattern Growth of Graphene Films for Stretchable Transparent Electrodes. *Nature* **2009**, *457*, 706–710.
- (3) Lipomi, D. J.; Vosgueritchian, M.; Tee, B. C. K.; Hellstrom, S. L.; Lee, J. A.; Fox, C. H.; Bao, Z. Skin-like Pressure and Strain Sensors Based on Transparent Elastic Films of Carbon Nanotubes. *Nat. Nanotechnol.* **2011**, *6*, 788–792.
- (4) Peng, H.; Dang, W.; Cao, J.; Chen, Y.; Wu, D.; Zheng, W.; Li, H.; Shen, Z. X.; Liu, Z. Topological Insulator Nanostructures for Near-Infrared Transparent Flexible Electrodes. *Nat. Chem.* **2012**, *4*, 281–286.
- (5) Kang, H.; Jung, S.; Jeong, S.; Kim, G.; Lee, K. Polymer-Metal Hybrid Transparent Electrodes for Flexible Electronics. *Nat. Commun.* **2015**, *6*, 6503.
- (6) Fan, F. R.; Tian, Z.-Q.; Wang, Z. L. Flexible Triboelectric Generator! *Nano Energy* **2012**, *1*, 328–334.
- (7) Wang, Z. L. Triboelectric Nanogenerators as New Energy Technology for Self-Powered Systems and as Active Mechanical and Chemical Sensors. *ACS Nano* **2013**, *7*, 9533–9557.
- (8) Fan, F. R.; Tang, W.; Wang, Z. L. Flexible Nanogenerators for Energy Harvesting and Self-Powered Electronics. *Adv. Mater.* **2016**, *28*, 4283–4305.
- (9) Niu, S.; Liu, Y.; Wang, S.; Lin, L.; Zhou, Y. S.; Hu, Y.; Wang, Z. L. Theory of Sliding-Mode Triboelectric Nanogenerators. *Adv. Mater.* **2013**, *25*, 6184–6193.
- (10) Jiang, T.; Zhang, L. M.; Chen, X.; Han, C. B.; Tang, W.; Zhang, C.; Xu, L.; Wang, Z. L. Structural Optimization of Triboelectric Nanogenerator for Harvesting Water Wave Energy. *ACS Nano* **2015**, *9*, 12562–12572.
- (11) Meng, B.; Tang, W.; Too, Z.-h.; Zhang, X.; Han, M.; Liu, W.; Zhang, H. A Transparent Single-Friction-Surface Triboelectric Generator and Self-Powered Touch Sensor. *Energy Environ. Sci.* **2013**, *6*, 3235–3240.
- (12) Tang, W.; Han, C. B.; Zhang, C.; Wang, Z. L. Cover-Sheet-Based Nanogenerator for Charging Mobile Electronics Using Low-Frequency Body Motion/Vibration. *Nano Energy* **2014**, *9*, 121–127.
- (13) Pang, Y.; Xue, F.; Wang, L.; Chen, J.; Luo, J.; Wang, Z. L. Tribotronic Enhanced Photoresponsivity of a MoS₂ Phototransistor. *Adv. Sci.* **2016**, *3*, 1500419.
- (14) Kim, S.; Gupta, M. K.; Lee, K. Y.; Sohn, A.; Kim, T. Y.; Shin, K. S.; Kim, D.; Kim, S. K.; Lee, K. H.; Shin, H. J.; Kim, D. W.; Kim, S. W. Transparent Flexible Graphene Triboelectric Nanogenerators. *Adv. Mater.* **2014**, *26*, 3918–3925.
- (15) Shin, S. H.; Kwon, Y. H.; Kim, Y. H.; Jung, J. Y.; Lee, M. H.; Nah, J. Triboelectric Charging Sequence Induced by Surface

Functionalization as a Method To Fabricate High Performance Triboelectric Generators. *ACS Nano* **2015**, *9*, 4621–4627.

(16) Yu, Y.; Li, Z.; Wang, Y.; Gong, S.; Wang, X. Sequential Infiltration Synthesis of Doped Polymer Films with Tunable Electrical Properties for Efficient Triboelectric Nanogenerator Development. *Adv. Mater.* **2015**, *27*, 4938–4944.

(17) Luo, J.; Fan, F. R.; Jiang, T.; Wang, Z.; Tang, W.; Zhang, C.; Liu, M.; Cao, G.; Wang, Z. L. Integration of Micro-Supercapacitors with Triboelectric Nanogenerators for a Flexible Self-Charging Power Unit. *Nano Res.* **2015**, *8*, 3934–3943.

(18) Niu, S.; Wang, X.; Yi, F.; Zhou, Y. S.; Wang, Z. L. A Universal Self-Charging System Driven by Random Biomechanical Energy for Sustainable Operation of Mobile Electronics. *Nat. Commun.* **2015**, *6*, 8975.

(19) Tang, W.; Zhou, T.; Zhang, C.; Fan, F. R.; Han, C. B.; Wang, Z. L. A Power-Transformed-and-Managed Triboelectric Nanogenerator and Its Applications in a Self-Powered Wireless Sensing Node. *Nanotechnology* **2014**, *25*, 225402.

(20) Hwang, B. U.; Lee, J. H.; Trung, T. Q.; Roh, E.; Kim, D. I.; Kim, S. W.; Lee, N. E. Transparent Stretchable Self-Powered Patchable Sensor Platform with Ultrasensitive Recognition of Human Activities. *ACS Nano* **2015**, *9*, 8801–8810.

(21) Fan, F. R.; Luo, J.; Tang, W.; Li, C.; Zhang, C.; Tian, Z.; Wang, Z. L. Highly Transparent and Flexible Triboelectric Nanogenerators: Performance Improvements and Fundamental Mechanisms. *J. Mater. Chem. A* **2014**, *2*, 13219–13225.

(22) Chandrashekar, B. N.; Deng, B.; Smitha, A. S.; Chen, Y.; Tan, C.; Zhang, H.; Peng, H.; Liu, Z. Roll-to-Roll Green Transfer of CVD Graphene onto Plastic for a Transparent and Flexible Triboelectric Nanogenerator. *Adv. Mater.* **2015**, *27*, 5210–5216.

(23) Luo, J.; Fan, F. R.; Zhou, T.; Tang, W.; Xue, F.; Wang, Z. L. Ultrasensitive Self-Powered Pressure Sensing System. *Extreme Mech. Lett.* **2015**, *2*, 28–36.

(24) Zhong, J.; Zhu, H.; Zhong, Q.; Dai, J.; Li, W.; Jang, S. H.; Yao, Y.; Henderson, D.; Hu, Q.; Hu, L.; et al. Self-Powered Human-Interactive Transparent Nanopaper Systems. *ACS Nano* **2015**, *9*, 7399–7406.

(25) Grzybowski, B. A.; Winkleman, A.; Wiles, J. A.; Brumer, Y.; Whitesides, G. M. Electrostatic Self-Assembly of Macroscopic Crystals Using Contact Electrification. *Nat. Mater.* **2003**, *2*, 241–245.

(26) Guo, H.; Leng, Q.; He, X.; Wang, M.; Chen, J.; Hu, C.; Xi, Y. A Triboelectric Generator Based on Checker-Like Interdigital Electrodes with a Sandwiched PET Thin Film for Harvesting Sliding Energy in All Directions. *Adv. Energy Mater.* **2015**, *5*, 1400790.

(27) Tang, W.; Zhang, C.; Han, C. B.; Wang, Z. L. Enhancing Output Power of Cylindrical Triboelectric Nanogenerators by Segmentation Design and Multilayer Integration. *Adv. Funct. Mater.* **2014**, *24*, 6684–6690.

(28) Yang, Y.; Jeong, S.; Hu, L.; Wu, H.; Lee, S. W.; Cui, Y. Transparent Lithium-Ion Batteries. *Proc. Natl. Acad. Sci. U. S. A.* **2011**, *108*, 13013–13018.

(29) Nam, I.; Park, S.; Kim, G. P.; Park, J.; Yi, J. Transparent and Ultra-Bendable All-Solid-State Supercapacitors without Percolation Problems. *Chem. Sci.* **2013**, *4*, 1663–1667.

(30) Toupin, M.; Brousse, T.; Belanger, D. Charge Storage Mechanism of MnO₂ Electrode Used in Aqueous Electrochemical Capacitor. *Chem. Mater.* **2004**, *16*, 3184–3190.

(31) Wei, W.; Cui, X.; Chen, W.; Ivey, D. G. Manganese Oxide-Based Materials as Electrochemical Supercapacitor Electrodes. *Chem. Soc. Rev.* **2011**, *40*, 1697–1721.

(32) Sun, L.; Wang, X.; Liu, W.; Zhang, K.; Zou, J.; Zhang, Q. Optimization of Coplanar High Rate Supercapacitors. *J. Power Sources* **2016**, *315*, 1–8.

(33) Lang, X.; Hirata, A.; Fujita, T.; Chen, M. Nanoporous Metal/Oxide Hybrid Electrodes for Electrochemical Supercapacitors. *Nat. Nanotechnol.* **2011**, *6*, 232–236.

(34) Sun, L.; Wang, X.; Zhang, K.; Zou, J.; Zhang, Q. Metal-Free SWNT/Carbon/MnO₂ Hybrid Electrode for High Performance Coplanar Micro-Supercapacitors. *Nano Energy* **2016**, *22*, 11–18.

(35) Niu, Z.; Zhou, W.; Chen, J.; Feng, G.; Li, H.; Hu, Y.; Ma, W.; Dong, H.; Li, J.; Xie, S. A Repeated Halving Approach to Fabricate Ultrathin Single-Walled Carbon Nanotube Films for Transparent Supercapacitors. *Small* **2013**, *9*, 518–524.

(36) Yuksel, R.; Sarioba, Z.; Cirpan, A.; Hiralal, P.; Unalan, H. E. Transparent and Flexible Supercapacitors with Single Walled Carbon Nanotube Thin Film Electrodes. *ACS Appl. Mater. Interfaces* **2014**, *6*, 15434–15439.

(37) Wu, Z.-S.; Parvez, K.; Feng, X.; Muellen, K. Graphene-Based In-Plane Micro-Supercapacitors with High Power and Energy Densities. *Nat. Commun.* **2013**, *4*, 2487.

(38) Chen, T.; Xue, Y.; Roy, A. K.; Dai, L. Transparent and Stretchable High-Performance Supercapacitors Based on Wrinkled Graphene Electrodes. *ACS Nano* **2014**, *8*, 1039–1046.